Simulation of the Tip Vortex Behind a Wing at Static and Dynamic Stall Conditions

May 26, 2008

Abstract

The behavior of the tip-vortex behind a square NACA0015 wing was numerically investigated. The problems studied include the stationary and the oscillating wing at static and dynamic stall conditions. Reynolds-averaged Navier-Stokes (RANS) and detached-eddy simulation (DES) schemes were implemented. Vortex structures predicted by RANS were mainly diffused while DES was able to produce qualitatively and quantitatively better results as compared to the experimental data. The break-up of the tip vortex, which started at the end of the upstroke and continued to the middle of the downstroke over an oscillation cycle, was observed in DES data.

1 Introduction

Reynolds-averaged Navier-Stokes (RANS) equations coupled with the turbulence model have been widely denounced for their poor performance to simulate separated flows. Yet another deficiency of the RANS methodology might arise while simulating main vortical flow features away from the wall such as the downstream evolution of a wing tip-vortex. The Spalart-Allmaras (SA) turbulence model, for instance, will generate excessive turbulent viscosity along the vortex axis as a results of the significant vorticity-generated production term accompanied with the diminishing destruction term away from the wall. Consequently, the resolution of the downstream tip vortex will be impaired due to the extreme dissipation.

With the increase of the computing power, the large eddy simulation (LES) method has gained popularity mainly because of producing high-fidelity flow simulation results in the separated regions. Meanwhile, the extremely fine mesh required to resolve the attached boundary layer regions hinders the use of LES in engineering and practical applications. As practical alternatives, hybrid RANS/LES methods have been developed to exploit advantageous qualities of RANS and LES in different

targeted regions of the flow field. In particular, Detached-eddy simulation (DES) method uses the RANS approach in attached boundary layers and the LES mode in separated flows. Since its first formulation based on SA model [24], DES has been validated on various geometries and flow conditions including circular or square cylinder [26], delta wing [6], airplane configuration [16], and the turbulent wake [1]. New formulations have been introduced to include other turbulence models such as k-ω SST [28] and LL k-ε [4], and modifications have been made to improve the performance of the model at ambiguous grid spacing and low Reynolds numbers [23]. As a result, DES has become one of the primary candidates for simulating massively separated flows.

In particular, DES can be considered as an appropriate simulation tool to investigate the behavior of the tip-vortex behind a wing under deep-stall oscillations. This problem requires the accurate prediction of two major flow features: the onset of the dynamic stall (DS) and the downstream evolution of the tip-vortex. Only few experimental work studying this problem exist in the literature [10, 5, 3, 2]. The related CFD literature has been mainly devoted to the study of DS phenomenon while the majority of the work deal with airfoil configurations. Ekaterinaris and Platzer [8] reviewed the CFD simulations of airfoil DS up to 1996. The 3D DS of the laminar flow around a NACA0015 wing was then simulated by Newsome [17] where little emphasis was given to the behavior of the tip-vortex under DS condition. Szydlowski and Costes [27] used RANS and DES methods to simulate the flow field around NACA0015 airfoil under static and dynamic stall. In a recent work by Spentzos et al [25], the 3D DS of turbulent flow around oscillating wings with various platforms was studied using RANS methodology. They also investigated the interaction of the tip-vortex with the DS vortices over the wing platform. However, no information was provided regarding the downstream evolution of the tip-vortex behind the wing.

The objective of this work is two fold. First, DES and RANS methods are evaluated to predict the onset of static and dynamic stall. Second, the downstream evolution of the tip vortex under DS oscillations are investigated. Throughout this study, RANS and DES results are compared with each other as well as the experimental data of Birch and Lee [3, 2] for a square NACA0015 wing. The mathematical and numerical models are described in section 2. The DES calibration and the simulation results for stationary and oscillating wings are presented in section 3. Conclusions and plans for the future work are given at the end.

2 Methodology

2.1 Mathematical Models

The unsteady turbulent aerodynamic flow is modeled by compressible Navier-Stokes (NS) equations. Turbulence effects are taken into account via an eddy-viscosity approach; whereby the kinematic viscosity and thermal conductivity, μ and k, are augmented by modeled turbulent (eddy) viscosity and turbulent thermal conductivity , μ_t and k_t, respectively. Molecular diffusion parameters μ and k are then replaced by $\mu + \mu_t$ and $k + k_t$ in NS equations. Turbulent thermal conductivity is calculated from turbulent viscosity with the assumption of a constant turbulent Prandtl number of $\mathrm{Pr}_t = \frac{c_p \mu_t}{k_t} = 0.9$.

The closure is achieved by solving the one-equation Spalart-Allmaras (SA) turbulence model [22] for the reduced eddy viscosity, $\tilde{\nu}$. The transport equation is given by,

$$\frac{D(\rho\tilde{\nu})}{Dt} = c_{b1}\rho\tilde{S}\tilde{\nu} + \frac{1}{\sigma}\nabla\cdot[(\rho\nu + \rho\tilde{\nu})\nabla\tilde{\nu}] + \frac{c_{b2}}{\sigma}\rho\left(\nabla\tilde{\nu}\right)^2 - c_{w1}\rho f_{w1}\left(\frac{\tilde{\nu}}{d}\right)^2. \quad (1)$$

Variables and functions presented in equation (1) are defined as below.

$$\nu_t = \tilde{\nu} f_{v1} \qquad f_{v1} = \frac{\chi^3}{\chi^3 + c_{v1}^3} \qquad \chi = \frac{\tilde{\nu}}{\nu};$$
$$\tilde{S} = S + \frac{\tilde{\nu}}{\kappa^2 d^2} f_{v2} \quad f_{v2} = 1 - \frac{\chi}{1 + \chi f_{v1}};$$
$$f_w = g\left(\frac{1 + c_{w3}^6}{g^6 + c_{w3}^6}\right)^{1/6} \quad g = r + c_{w2}(r^6 - r) \quad r = \frac{\tilde{\nu}}{\tilde{S}\kappa^2 d^2}.$$

where constants c_{b1}, c_{b2}, c_{w1}, c_{w2}, c_{w3}, c_{v1}, and κ have the same values as those indicated by Spalart et al. [22].

In the course of the LES calibration as described in section 3.1, we have also implemented Smagorinsky sub-grid scale (SGS) model where the turbulent viscosity is given by an algebraic relation,

$$\nu_t = (C_S\Delta)^2\|S\|. \quad (2)$$

Model constant, grid spacing and flow strain tensor are represented by C_S, Δ, and S_{ij} respectively.

For the treatment of moving or deformable meshes, the governing equations of the flow and turbulent viscosity are reformulated based on the arbitrary Lagrangian-Eulerian (ALE) kinematical description of the fluid domain [7].

2.2 Computational Methods

2.2.1 Space-Time Discretization

The flow and turbulence model equations are discretized with a hybrid finite-volume-finite-element method [11], which is accompanied by the discretization of the computational domain into unstructured tetrahedral elements and the construction of median-dual control volumes around mesh vertices. Convective fluxes are calculated using the second-order upwind Roe scheme whereas diffusive and source terms are discretized with linear finite element shape functions.

NS and SA equations are loosely coupled during the computation, i.e. NS equations are solved first, then turbulence viscosity is updated using recently calculated values of the flow variables.

The time integration is performed via a second-order accurate implicit scheme; the non-linear fluxes are linearized by applying the Newton method and introducing flux Jacobian matrices. Geometric conservation laws developed by Lesoinne et al. [15] and Farhat et al. [9] are implemented for the time integration of the convective fluxes in moving or deformable meshes while the corresponding Jacobians are calculated at the intermediate mesh positions described by Nkonga et al. [18]. Since the construction of a spatially second-order accurate convective Jacobian is difficult, only a first-order approximation is used. For time accurate unsteady simulations, the spatial accuracy is then improved by performing two or three Newton iterations at each time step [20].

2.2.2 Iterative Solver and Preconditioning

The linear system of equations resulted from aforementioned discretization schemes is solved with preconditioned (block Jacobi) Generalized minimal residual method (GMRES) [19]. To improve the convergence of the flow solver at low Mach numbers, the local low-speed preconditioner of Turkel [29] is implemented. The low-speed modifications for the Roe scheme (Roe-Turkel scheme [30]) are performed at two levels: preconditioning of the temporal term (iterative preconditioning) and preconditioning of the upwind term. The first stage enhances the convergence rate, the second improves the accuracy of the solution at low Mach numbers. To preserve the time accuracy required for unsteady flow simulations, the low-speed preconditioning is always performed in the context of multiple Newton iterations per time step.

2.2.3 Detached-Eddy Simulation

The Delayed DES (DDES) model of Spalart et al. [23] based on the SA equation (1) is implemented to the flow solver. SA-DDES and its older version SA-DES97 [24] is built by replacing the distance to the solid wall, d, in equation (1) with a smaller

length scale $\tilde{d}$. This modification results in a bigger destruction term and hence reduces the modeled turbulent viscosity, ν_t, in the separation regions and away from the solid wall where the flow is dominated by 3D vortical structures (LES regions). In DDES, $\tilde{d}$ is given by [23],

$$\tilde{d} = d - f_d \mathrm{MAX}(0, d - C_{DES}\Delta). \tag{3}$$

The value of constant C_{DES} will be determined, in section 3.1 by simulating the decay of isotropic turbulence (DIT) in a periodic box and calibrating the simulation results with the available direct numerical simulation (DNS) data. The function f_d should be around 1 in the LES region and almost 0 in the attached boundary layer (RANS region) as well as irrotational zones. Its value depends on the non-dimensional parameter r_d. The parameter and the function are defined by Spalart et al. [23] as,

$$r_d = \frac{\tilde{\nu}}{\sqrt{U_{i,j}U_{i,j}}\kappa^2 d^2}, \tag{4}$$

$$f_d = 1 - \tanh\left(8^3 r_d^3\right), \tag{5}$$

where $U_{i,j}$ is the tensor of velocity gradients. For each mesh vertex (control volume), the length scale Δ is defined, herein, as the length of the longest edge connected to this vertex. In unstructured median-dual control volumes, this represents the largest distance between the center of the control volume under consideration and the center of its neighboring control volumes.

The numerical dissipation of upwind methods tends to impair the resolution of the turbulence coherent structures by strongly dissipating the turbulent kinetic energy in medium size eddies. The common practice is to scale down the amount of the numerical dissipation of the scheme in the LES regions. Travin et al. [28] developed a blending function that allows upwind formulation to be active in high vorticity and fine grid areas. While Barone et al. [1] used Harten's artificial compression method (ACM) to adjust the magnitude of the numerical dissipation. In this paper, the upwind part of the Roe flux is scaled as follows,

$$\mathbf{F}^{ij}_{Roe} = \frac{1}{2}(\mathbf{F}_i + \mathbf{F}_j) - \frac{1}{2}\sigma\mathbf{R}|\mathbf{\Lambda}|\mathbf{L}(\mathbf{U}_j - \mathbf{U}_i), \tag{6}$$

where the scaling parameter σ is obtained from function f_d as,

$$\sigma = 1 - f_d. \tag{7}$$

In section 3.1, a slightly modified version of relation (7) will be introduced.

All numerical algorithms described in this section is parallelized using the message passing standard (MPI).

3 Results

3.1 Decay of Isotropic Turbulence: Calibration of LES Mode

The simulation results for the decay of isotropic turbulence in a periodic box is compared with the DNS data of the AGARD LES validation database [13]. The computational domain consisted of a cube with equal edge lengths of 2π. Periodic boundary condition was applied to each three pairs of facing sides of the cube. Two different mesh resolutions were studied; the coarse and fine meshes contained 32^3 and 64^3 uniform cubes respectively. Each cube was then divided into six tetrahedral elements. Comparisons are made between the calculated 3D energy spectra at a non-dimensional time of 2.018.

The calibration steps described by Bunge et al. [4] were followed. First, the calibration was performed for Smagorinsky model, whereby the optimal value for constant C_s as well as upwinding parameter σ were obtained. The upwinding parameter in equation (6) was kept constant throughout the computational domain. As depicted in Figure 1-a, $\sigma = 0.015$ was the optimal value 64^3 resolution with $C_s = 0.15$. The optimal value of C_s was strongly dependent on the grid resolution. For the coarse mesh, $C_s = 0.19$ gave the best result.

At the second stage, detached-eddy simulations were performed where SA turbulence model replaced Smagorinsky SGS model. The proper initialization of the turbulence viscosity field was achieved as follows [4]: the Smagorinsky model was used to obtain the initial guess for the distribution of the eddy viscosity in the domain. SA equation was then solved while the flow field was kept frozen till convergence. The DIT simulation began afterward. The turbulent 3D energy spectra at various C_{DES} constants ares shown in Figure 1-b. Unlike the Smagorinsky constant, C_{DES} is less sensitive to the grid resolution. We have selected $C_{DES} = 0.51$ as the optimal value. Finally, another simulation was performed in which C_{DES} was kept at its optimal value while the upwinding parameter was calculated from equation (7) and limited as,

$$\sigma = MAX(0.015, 1 - f_d). \tag{8}$$

The energy spectra and flow field were similar to those with constant value of $\sigma = 0.015$. This indicated the proper behavior of the function f_d, which took values close to 1 in the entire DIT box (LES region).

The second norm of the residual was reduced up to six order of magnitude in GMRES iterations. Two Newton iterations were performed at each time step. Increasing the number of Newton iterations had no significant results in the time evolution of the turbulent 3D energy spectra.

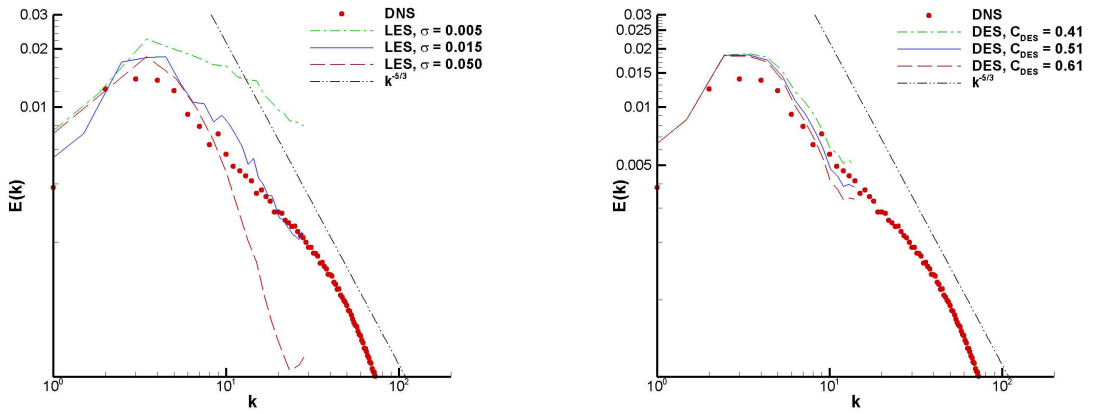

Figure 1: Calibration of parameters in Smagorinsky LES and DES schemes with DNS data [13] for DIT problem. **a** 3D energy spectra in 64^3 cube at a nondimensional time of 2.018 for different upwinding parameter using Smagorinsky SGS model with $C_s = 0.15$. **b** 3D energy spectra in 32^3 cube at a nondimensional time of 2.018 for different C_{DES} parameter using DES model with $\sigma = 0.015$.

3.2 NACA0015 Wing

3.2.1 Overview

The structure of the tip vortex generated by a square NACA0015 wing was numerically studied using RANS and DES methods. The problems considered include the stationary wing fixed at various angles of attack (AOA) and the wing in pitching oscillations. These problems were experimentally investigated by Birch and Lee [3, 2]. They measured velocity components at grid points with uniform spacing of 3.2 mm on a rectangular plane located at $x/c = 1$. In our numerical study, we interpolated the velocity components on the similar grid points from the simulated flow filed. Our purpose is to compare the performance of RANS and DES models to predict the near-field structure of the tip vortex and the onset of the static and dynamic stall. For the vortex visualization in the 3D flow field, we adopted the λ_2 method of Jeong and Hussain [12].

3.2.2 Wing Configuration and Mesh

The test case consisted of a rectangular, square-tipped NACA0015 half wing with chord and half-span sizes of 0.203 m and 0.508 m, respectively. The wing was attached to a free-slip wall at the root section. This geometry was slightly different from the one used for experimental studies where the root was attached to an end-plate, which, in turn, was located close to the wind tunnel wall [3, 2]. The wing configuration is depicted in Figure 2. The origin of the Cartesian coordinate system was placed at the trailing edge of the wing at the tip section with its x and z-axes along the chord line and the span of the wing, respectively. For the oscillating wing, the above orientation corresponded to the wing at the mean incidence angle. The pitching axis passed through the quarter-chord points and was parallel to the z-axis.

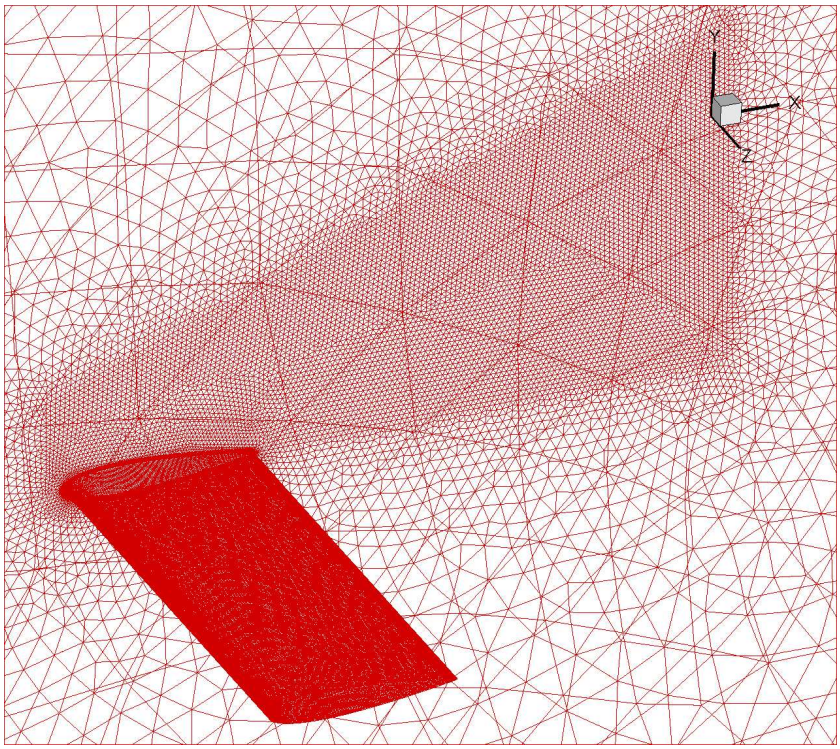

Figure 2: Unstructured tetrahedral mesh around NACA0015 wing with $2,247,174$ nodes and $13,300,570$ elements. The focus region of DES appears in the figure as the dense trapezoidal region above the wing, which contains $5,308,217$ elements.

The freestream velocity was equal to 14.4 m/s, which resulted in a chord Reynolds number of 1.86×10^5. The stationary simulations were performed at four AOAs of $\alpha = 12.0°$, $14.0°$, $16.0°$, and $18.0°$; whereas, the non-stationary simulation

involved pitching oscillations with a reduced frequency of 0.09, a mean incidence angle of 18.0°, and an amplitude of 6.0°, i.e. $\alpha = 18.0° + 6.0° \sin(\omega t)$.

The computational mesh shown in Figure 2 contained $2,247,174$ nodes and $13,300,570$ tetrahedral elements. As described by Spalart [21], the computational domain was divided into several target regions addressing different modeling schemes. Tetrahedral elements were constructed by triangulation of semi-structured prism layers in the RANS region (RR). The grid spacing from the wall, in the first, layer satisfied $y^+ \approx 1$ in the law-of-wall units. The focus region (FR), which can be distinguished, in Figure 2, as the dense area above the wing, contained an almost isotropic mesh with a uniform edge size of $0.028c$. This region was connected to an Euler region (ER) through a small departure region (DR). The maximum size of the mesh edges in the ER was limited to c. A finer grid with $21,134,220$ tetrahedra, was built via grid refinement by a factor of $\sqrt{2}$ in the FR to examine whether the coarse simulation results were sufficiently resolved. The time step for the stationary and oscillating wing simulations was $0.0078c/U_\infty$. The coarse and fine grids were decomposed into 46 and 64 subdomains using METIS [14]. Although RANS requirements for mesh and time step are generally less stringent than DES', the same mesh and time step were used for RANS simulations to make a fair assessment of the accuracy of each scheme for unsteady flow simulations.

3.2.3 Stationary Wing

Figures 3 compares DES results to RANS solutions for the static wing at $\alpha = 18°$. Both simulations were performed on the coarse grid. DES, figure 3-a, predicted a completely detached flow from the inboard part of the wing upper surface leading to the vortex shedding. RANS, figure 3-b, failed to predict the shedding of vortices. However, a strong trailing edge vortex was resolved with a flow reversal that extended from the trailing edge up to $0.2c$ in the inboard region, figure 4. The flow detachment or reversal gradually diminished toward the wing tip in the in DES and RANS solutions. Furthermore, due to the excessive dissipation, the RANS model predicted a thicker and more diffused tip vortex, as depicted in figures 3. The $x/c = 1$ data plane crossing the tip vortex is depicted in the same figures.

2D vorticity contours at the $x/c = 1$ plane are compared in Figure 5. DES results were averaged over 100 time steps. The peak value of nondimensional vorticity calculated in the experiment [2] was 23. Here again RANS predicted a significantly lower value for the maximum vorticity.

Maximum vorticity, maximum tangential velocity, and vortex core radius versus four angles of attack at $x/c = 1$ plane are shown in Figure 6. The core radius was measured as the distance between the location of the maximum tangential velocity and the center of the vortex. DES results for all three parameters lay between RANS solutions and the experimental data [3]; a significant improvement was obtained to

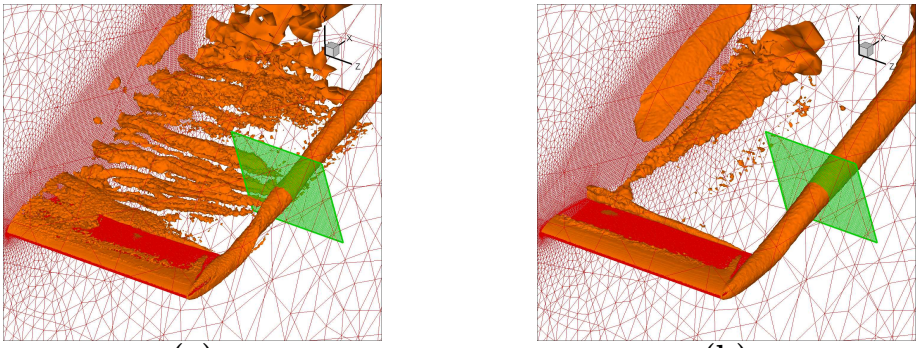

Figure 3: λ_2 iso-surfaces in flow around stationary NACA0015 wing at $\alpha = 18°$. **a** DES results. **b** RANS results.

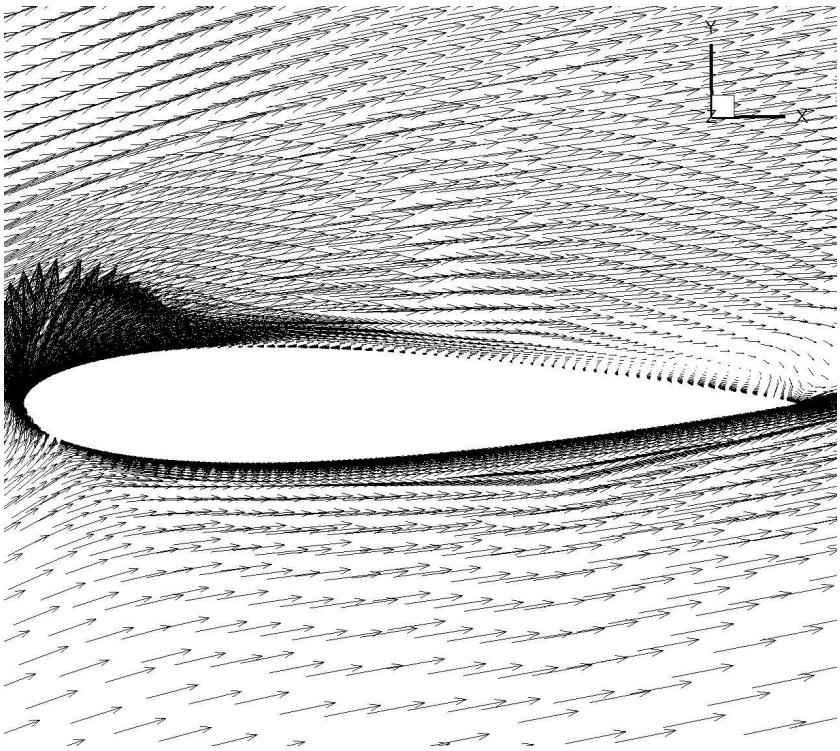

Figure 4: Vector plot at the root section for the flow around stationary NACA0015 wing at $\alpha = 18°$ simulated using RANS method.

better predict the tip-vortex configuration at $x/c = 1$.

The onset of the static stall is investigated in Figure 7 where the vortex field

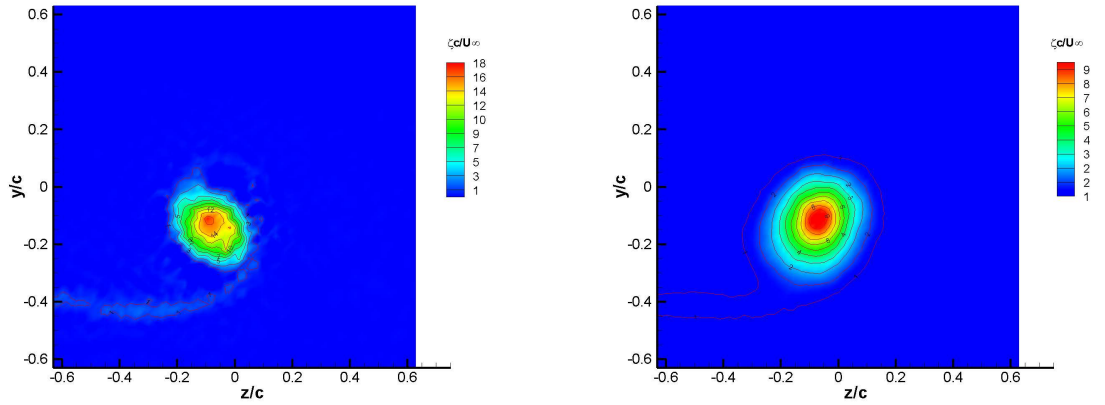

Figure 5: Vorticity contours at $x/c = 1$ in flow around stationary NACA0015 wing at $\alpha = 18°$. **a** DES results. **b** RANS results.

around NACA0015 wing is shown at three static AOAs of 12°, 14°, and 16°. At $\alpha = 12°$, Figure 7-a, the flow was entirely attached to the wing surface. The flow separation at the trailing edge and the resulting trailing edge vortex were observed at $\alpha = 14°$ in Figure 7-b. Further increase of the AOA to 16° led to the massive separation of the flow over the inboard part of the wing upper surface and the vortex shedding as depicted in Figure 7-c. The approximate static stall AOA would therefore lie between 14° and 16°, i.e., $14° < \alpha_{ss} < 16°$. This complies with the experimental measurement [2] in which $\alpha_{ss} \approx 15°$. As it was seen earlier in Figure 3, RANS failed to predict the vortex shedding. Furthermore, its predicted static stall angle was greater than 16°.

3.2.4 Oscillating Wing

The dynamic stall of the NACA0015 wing in pitching oscillations was simulated. Before the presentation of the results, two points should be clarified:

1. A phase-lag compensation scheme was employed in the experimental studies of Birch and Lee [3, 2] to modify the instantaneous position of the wing at the moment of the flow measurement. This compensation was intended to take into account the phase-lag that exists for the flow structure to move from the wing to the location of the velocity sensors ($x/c = 1$ plane). In this section, whenever we examine only simulation results (DES and/or LES), the

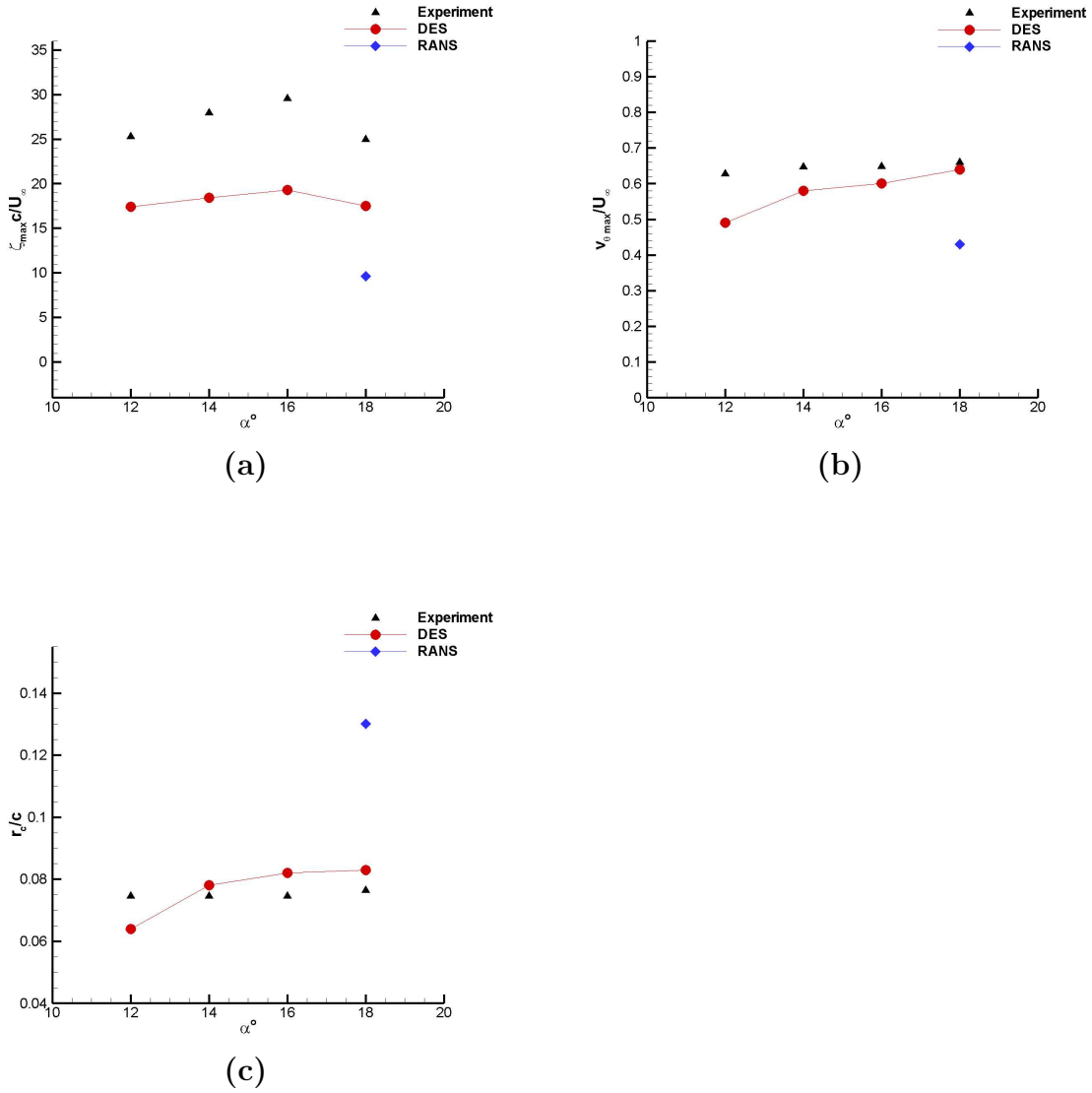

Figure 6: Variation of vortex parameters with AOA at $x/c = 1$ plane and comparison with the experimental data [3] for the flow around stationary NACA0015 wing. **a** Maximum vorticity. **b** Maximum tangential velocity. **c** Core radius.

reported wing angles are not compensated. This helps us investigate the vortex flow-structure during the oscillation cycle without being involved with the discrepancies that exist between different compensation schemes. Whereas, in the graphs that include comparisons between simulation and experimental

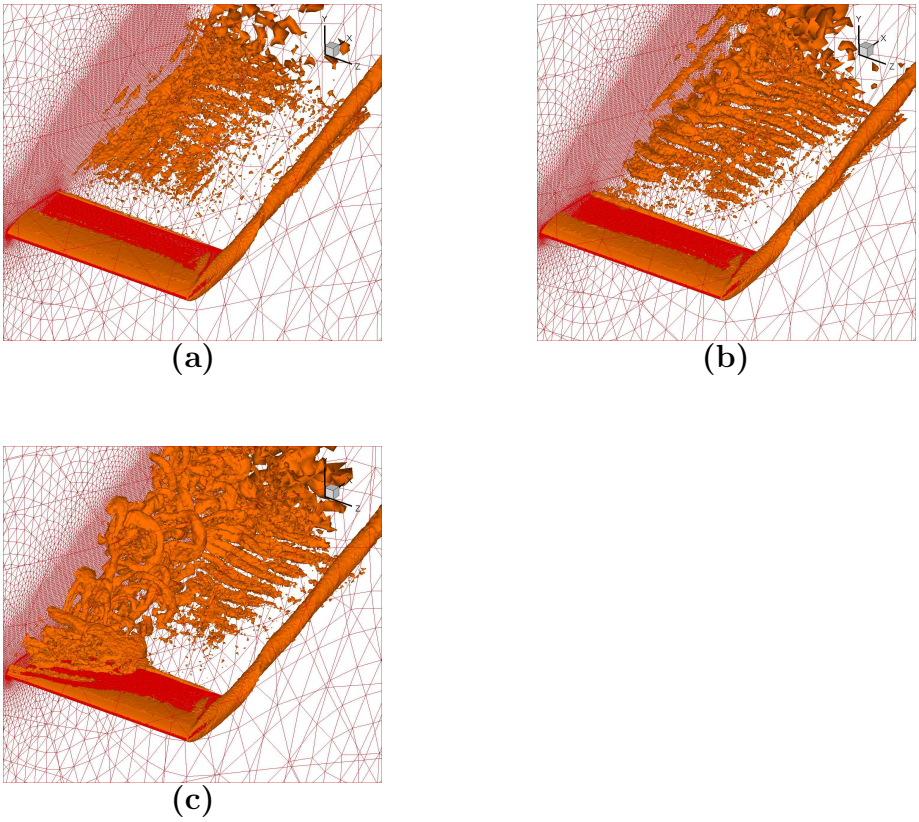

Figure 7: λ_2 iso-surfaces around static NACA0015 wing at three AOAs of 12°, 14°, and 16°. **a** $\alpha = 12°$. **b** $\alpha = 14°$. **c** $\alpha = 16°$.

data, for the sake of consistency, the same phase-lag compensation scheme as the one used by Birch and Lee was implemented;

2. The simulation results presented in this section are instantaneous quantities calculated at various wing positions. The reported experimental data were, on the contrary, the ensemble averages over 40-80 pitching cycles at the corresponding positions. In DES, calculating the phase-locked averages of the flow quantities even over few cycles is computationally very expensive (each DES cycle takes more than three weeks in current computations). Although RANS simulations are significantly less expensive than DES, the calculated flow quantities exhibited very little changes over different cycles except for the first transient quarter cycle. Due to the high computational cost for DES and the lack of the significance for RANS, only the instantaneous flow quantities at specified wing positions were presented.

The structure of the tip vortex and turbulent eddies resulted from the flow separation in DES and RANS solutions are shown in Figure 8-a–e where pitch-up and pitch-down strokes are distinguished by subscripts u and d, respectively. Turbulent eddies in the RANS solutions, similar to the static wing simulation, were highly diffused. The cloud like structures were formed as the excessive numerical diffusion merged these eddies into each other and made the resolution of small eddy structures impaired. The strong tip vortex was also diffused and had a bigger diameter than the one in the DES solution.

The following unsteady flow behaviors were observed for DES in a pitching cycle: during the pitch-up from $\alpha = 12^\circ_u$ to $\alpha = 16^\circ_u$, the flow was mainly attached, Figure 8-a. A small region of the flow reversal appeared at the inboard area of the wing trailing edge at the end of this period, Figure 8-b. This flow reversal expanded more toward the outboard region and the leading edge from $\alpha = 16^\circ_u$ to $\alpha = 22^\circ_u$, Figure 8-c. Meanwhile, the leading edge vortex (LEV) was formed and grew up. The dynamic stall started at $\alpha \approx 22^\circ_u$, which was characterized by the massive separation region covering most of the wing upper surface, Figure 8-d. The dynamic stall condition continued until $\alpha \approx 20^\circ_d$. The flow reattachment began afterward, Figure 8-e, and proceeded gradually until the complete reattachment of the flow at the lower peak of the pitching cycle. The DES prediction of the deep-stall oscillation was in good agreement with the reported experimental observation [3]. RANS predictions are depicted in Figures 9-a–e, where more and less the same qualitative behaviors for the onset of the flow separation and reattachment were observed. The massive separation region in RANS, Figure 9-d, was more limited to the inboard part of the wing and smaller than the similar region in DES.

Furthermore, DES predicted the break-up of the tip-vortex, which began during the pitch-up between 23°_u and 24°. The tip-vortex restored to its original uniform structure much later at $\alpha \approx 16^\circ_d$. The distorted tip vortex during the pitch-down at $alpha = 18^\circ_d$ is depicted in Figure 8-e. RANS failed to capture this break-up. Since only velocity components of the flow were measured on some fixed data planes corresponding to different x/c locations in the experimental study, the vortex break-up was not explicitly reported by Birch and Lee. However, the effect of it was seen and pointed out in the phase-locked ensemble averaged data as the highly diffused vortex, the lack of axisymmetry, and lower values of vorticity.

4 Conclusion

Static and dynamic stalls of a NACA0015 wing and the behavior of its tip-vortex at $x/c = 1$ plane were numerically investigated. DES and RANS methodology were implemented. DES outperformed RANS in predicting the onset of the static stall, flow characteristics over an oscillation cycle, and the tip-vortex configuration

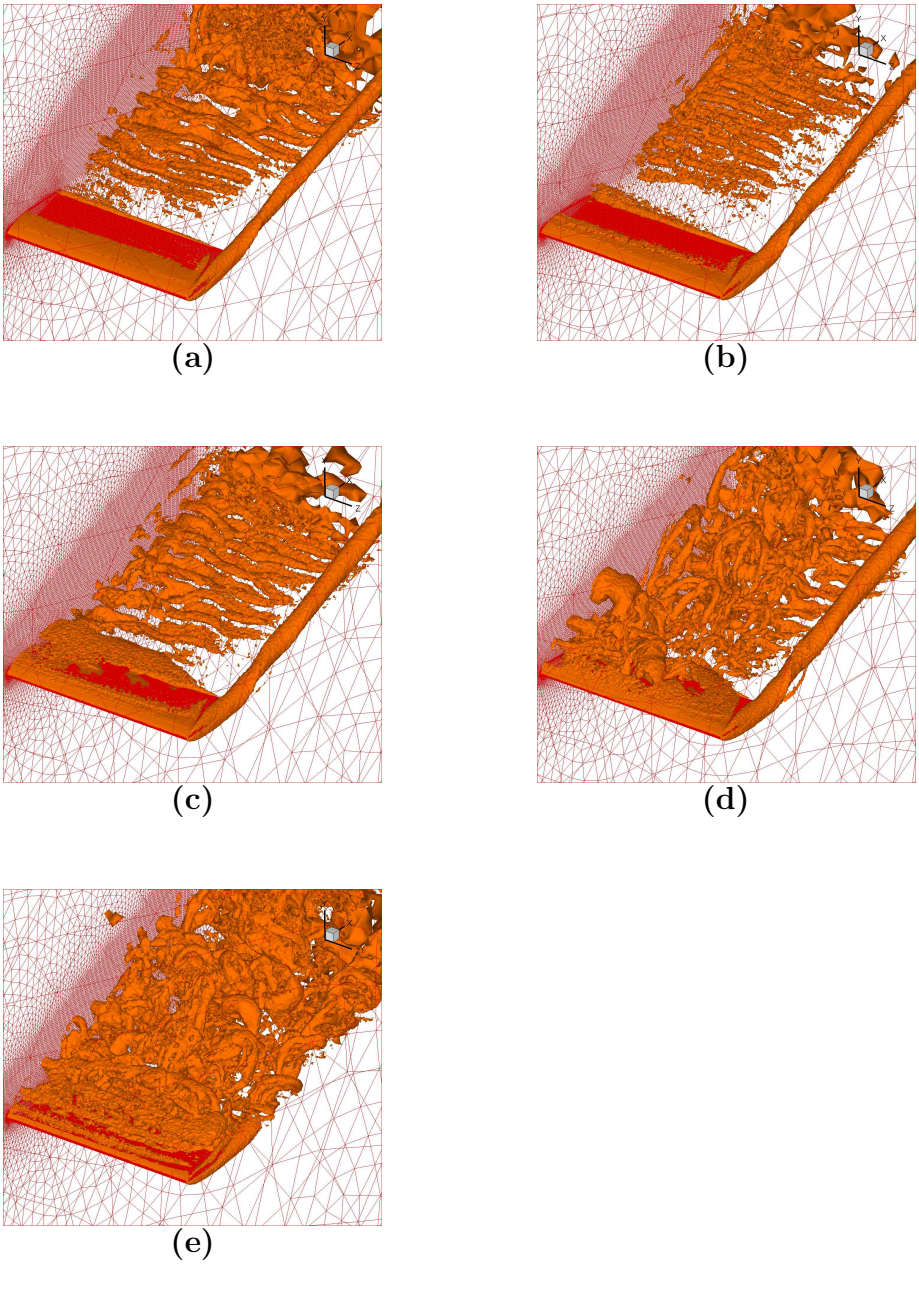

Figure 8: DES predictions for λ_2 iso-surfaces around oscillating NACA0015 wing at various pitching angles, $\alpha = 18^\circ + 6^\circ \sin(\omega t)$. **a** $\alpha = 12^\circ_u$. **b** $\alpha = 16^\circ_u$. **c** $\alpha = 19^\circ_u$. **d** $\alpha = 22^\circ_u$. **e** $\alpha = 18^\circ_d$

at the designated downstream location. The main shortcoming of DES was the

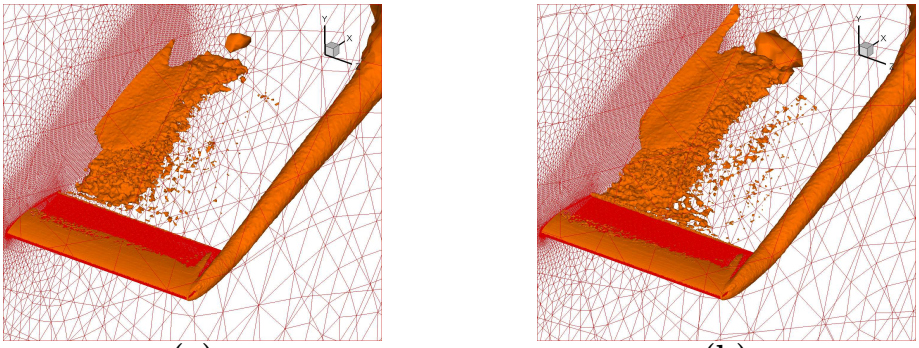

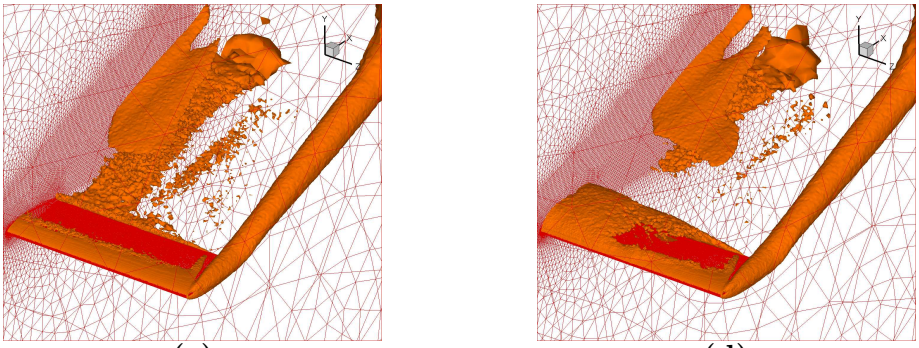

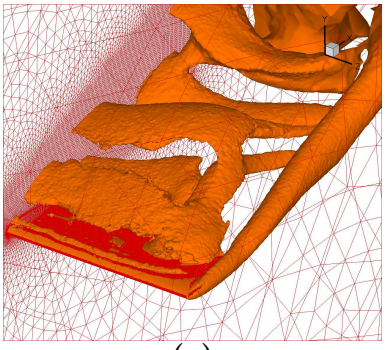

Figure 9: RANS predictions for λ_2 iso-surfaces around oscillations NACA0015 wing at various pitching angles, $\alpha = 18^\circ + 6^\circ \sin(\omega t)$. **a** $\alpha = 12^\circ_u$. **b** $\alpha = 16^\circ_u$. **c** $\alpha = 19^\circ_u$. **d** $\alpha = 22^\circ_u$. **e** $\alpha = 18^\circ_d$

computational time; each DES time-step was, on average, five times as expensive as

the similar RANS time-step.

More results, including the comparison of the vortex configuration behind the oscillating wing with the experimental data, will be added to the final paper.

References

[1] Matthew F. Barone and Christopher J. Roy. Evaluation of detached eddy simulation for turbulent wake applications. *AIAA Journal*, 44(12):3062 – 3071, 2006.

[2] D. Birch and T. Lee. Investigation of the near-field tip vortex behind an oscillating wing. *Journal of Fluid Mechanics*, 544:201 – 241, 2005.

[3] D. Birch and T. Lee. Tip vortex behind a wing undergoing deep-stall oscillation. *AIAA Journal*, 43(10):2081 – 2092, 2005.

[4] Ulf Bunge, Charles Mockett, and Frank Thiele. Guidelines for implementing detached-eddy simulation using different models. *Aerospace Science and Technology*, 11(5):376 – 385, 2007.

[5] Jo Won Chang and Seung O Park. Measurements in the tip vortex roll-up region of an oscillating wing. *AIAA Journal*, 38(6):1092 – 1095, 2000.

[6] S. Crippa and A. Rizzi. Initial steady/unsteady CFD analysis of vortex flow over the VFE-2 delta wing. In *Proceedings, 25th International Congress of the Aeronautical Sciences, ICAS*, 2006.

[7] J. Donea, S. Giuliani, and J. P. Halleux. Arbitrary Lagrangian-Eulerian finite element method for transient dynamic fluid-structure interactions. *Computer Methods in Applied Mechanics and Engineering*, 33(1-3):689 – 723, 1981.

[8] John A. Ekaterinaris and Max F. Platzer. Computational prediction of airfoil dynamic stall. *Progress in Aerospace Sciences*, 33(11-12):759 – 846, 1997.

[9] C. Farhat, M. Lesoinne, and P. Stern. High performance solution of three-dimensional nonlinear aeroelastic problems via parallel partitioned algorithms: methodology and preliminary results. *Advances in Engineering Software*, 28(1):43 – 61, 1997.

[10] P. Freymuth, W. Bank, and F. Finaish. Visualization of wing tip vortices in accelerating and steady flow. *Journal of Aircraft*, 23(9):731 – 733, 1986.

[11] L. Hallo, C. Le Ribault, and M. Buffat. Implicit mixed finite-volume-finite-element method for solving 3D turbulent compressible flows. *International Journal for Numerical Methods in Fluids*, 25(11):1241 – 1261, 1997.

[12] Jinhee Jeong and Fazle Hussain. On the identification of a vortex. *Journal of Fluid Mechanics*, 285:69 – 94, 1995.

[13] J. Jiminez. A selection of test cases for the validation of large-eddy simulations of turbulent flows. ftp://torroja.dmt.upm.es/AGARD/.

[14] G. Karypis and V. Kumar. A software package for partitioning unstructured graphs, partitioning meshes, and computing fill-reducing ordering of sparse matrices. Technical report, University of Minnesota, Department of Computer Science/Army HPC Research Center, 1998.

[15] Michel Lesoinne and Charbel Farhat. Geometric conservation laws for flow problems with moving boundaries and deformable meshes, and their impact on aeroelastic computations. *Computer Methods in Applied Mechanics and Engineering*, 134(1-2):71 – 90, 1996.

[16] Scott A. Morton, Denis Kholodar, Thomas Billingsley, James R. Forsythe, Kenneth E. Wurtzler, Kyle D. Squires, Russell M. Cummings, and Philippe R. Spalart. Multidisciplinary applications of detached-eddy simulation to separated flows at high reynolds numbers. In *Proceedings - Department of Defense High Performance Computing Modernization Program Users Group Conference, UGC 2004*, pages 103 – 111, Williamsburg, VA, United States, 2004.

[17] R.W. Newsome. Navier-stokes simulation of wing tip and wing juncture interactions for a pitching wing. *AIAA paper 94-2259*, 1994.

[18] R. Nkonga and H. Guillard. Godunov type method on non-structural meshes for three-dimensional moving boundary problems. *Computer Methods in Applied Mechanics and Engineering*, 113(1-2):183 – 204, 1994.

[19] Yousef Saad. *Iterative Methods for Sparse Linear Systems*. Society for Industrial and Applied Mathematics SIAM, 3600 University City Science Center, Philadelphia, PA 19104-2688, second edition, 2003.

[20] M. Sarkis and B. Koobus. A scaled and minimum overlap restricted additive schwarz method with application to aerodynamics. *Computer Methods in Applied Mechanics and Engineering*, 184(2-4):391 – 400, 2000.

[21] P.R. Spalart. Young-person's guide to detached-eddy simulation grids. Technical report, NASA/CR-2001-211032, 2001.

[22] P.R. Spalart and S.R. Allmaras. One-equation turbulence model for aerodynamic flows. *Recherche Aerospatiale*, 1:5 – 21, 1994.

[23] P.R. Spalart, S. Deck, M.L. Shur, K.D. Squires, M.Kh. Strelets, and A. Travin. A new version of detached-eddy simulation, resistant to ambiguous grid densities. *Theoretical and Computational Fluid Dynamics*, 20(3):181 – 195, 2006.

[24] P.R. Spalart, W.-H. Jou, M. Strelets, and S.R. Allmaras. Comments on the feasibility of les for wings, and on a hybrid rans/les approach. In *Proceedings - First AFOSR International Conference on DNS/LES*, pages 137 – 147, Ruston, Louisiana, United States, 1997.

[25] A. Spentzos, G.N. Barakos, K.J. Badcock, B.E. Richards, F.N. Coton, R. A. McD Galbraith, E. Berton, and D. Favier. Computational fluid dynamics study of three-dimensional dynamic stall of various planform shapes. *Journal of Aircraft*, 44(4):1118 – 1128, 2007.

[26] Kyle D. Squires, James R. Forsythe, and Philippe R. Spalart. Detached-eddy simulation of the separated flow over a rounded-corner square. *Journal of Fluids Engineering, Transactions of the ASME*, 127(5):959 – 966, 2005.

[27] J. Szydlowski and M. Costes. Simulation of flow around a naca0015 airfoil for static and dynamic stall configurations using rans and des. In *AHS International 4th Decennial Specialists' Conference on Aeromechanics*, pages 223 – 238, San Francisco, CA, United States, 2004.

[28] A. Travin, M. Shur, M. Strelets, and P.R. Spalart. Physical and numerical upgrades in the detached-eddy simulation of complex turbulent flows. In *Advances in LES of Complex Flows*, pages 239 – 254. Springer, 2002.

[29] E. Turkel and V.N. Vatsa. Local preconditioners for steady and unsteady flow applications. *Mathematical Modelling and Numerical Analysis*, 39(3):515 – 35, 2005.

[30] Cécile Viozat. Implicit upwind schemes for low mach number compressible flows. Rapport, Institute National de Recherche en Informatique et en Automatique, INRIA, January 1997.